Properties of TiO_2 Support and the Performance of Au/TiO_2 Catalyst for CO Oxidation Reaction

K.Y. Ho[a,b] and K.L. Yeung[b,*]

[a] Environmental Engineering Program and
[b] Department of Chemical Engineering, the Hong Kong University of Science and Technology, Clear Water Bay, Kowloon, Hong Kong
*Corresponding author.
Telephone no.: (852) 2358 7123
Fax: (852) 2358 0054
E-mail: kekyeung@ust.hk

Abstract

Gold catalysts were prepared on TiO_2 supports of different phase structures (i.e., anatase, rutile and biphasic), TiO_2 crystal size (i.e., 9-23 nm), surface and textural properties (i.e., hydration and surface area). The CO oxidation on the gold catalysts was carried out in an operando-DRIFTS set-up equipped with DRIFTS reactor cell connected on-line to CO gas analyser and gas chromatograph enabling real time monitoring of surface reaction and simultaneous reaction rate measurements. Gold catalysts supported on pure anatase TiO_2 were more resistant to sintering compared to catalysts supported on rutile and bi-phasic TiO_2. Besides catalyst sintering, deposition of surface carbonates is an important cause of catalyst deactivation. The best gold catalyst was prepared on 13 nm anatase TiO_2. It displays both increased activity and stability for CO oxidation reaction at room temperature. Surface and textural properties of TiO_2 also play a role on the performance of the Au/TiO_2 catalyst.

Keywords

gold, titanium dioxide, carbon monoxide, oxidation, operando-DRIFTS.

Introduction

Supported gold catalysts display excellent catalytic activity for CO oxidation at low temperatures (1-7). The biphasic Degussa P25 (75% anatase and 25% rutile TiO_2) is commonly used as support material and had been subject of many studies (8-13). It has been independently shown that the metal-support interface plays an important role of the catalytic activity and stability of Au/TiO_2 catalysts (14, 15). The recent work of Zhang *et al.* (16) reported the use of nanometer-sized zirconia dramatically increased the interfacial contact between gold and zirconia and greatly improved the catalytic activity of Au/ZrO_2 for CO oxiation. Pietron and Rolison (17, 18) attributed the high activity of gold-titania composite aerogel to the larger Au-TiO_2 interface.

Little is known about the effects of phase structure, crystal size, surface and textural properties on the catalytic performance Au/TiO_2 catalyst for CO oxidation reaction. Yan and coworkers (19) reported in a recent publication that catalytic activity of gold catalysts prepared on TiO_2 behaves in the order of brookite > anatase >> rutile. Moreau and Bond (20) prepared gold catalysts on anatase TiO_2 with surface area between 10 and 350 m^2g^{-1}. They reported the optimum catalyst was prepared from TiO_2 with a specific surface area 37 m^2g^{-1}. However, the work did not describe in detail the TiO_2 size, shape, and crystallinity. This work attempts to understand the effects of support phase structure (i.e., anatase and rutile), crystal size, surface and textural properties on the catalytic activity of Au/TiO_2 catalysts for CO oxidation reaction. Gold reference catalyst (GRC-A) supplied by World Gold Council was used for comparison. The reaction was conducted in a diffuse reflectance infrared Fourier transformed reaction cell equipped with on-line CO gas analyser and gas chromatograph. The operando-DRIFTS enabled the simultaneous monitoring of surface reaction and reaction rate measurements.

2 Experimental

2.1 Preparation of Au/TiO_2 Catalysts

Several gold catalysts were prepared on TiO_2 supports of different phase structures, crystal sizes, surface and textural properties. The synthesis procedure for nanostructured TiO_2 was reported in the previous works of Yeung *et al.* (21-25), where the TiO_2 crystal and aggregate sizes (21), crystallinity (22, 23) as well as surface properties (24, 25) can be manipulated during the synthesis. The preparation of TiO_2 supports were carried out in a N_2 dry box at room temperature. Titanium isopropoxide (TIP, 98 %, Acros Organics) dissolved in isopropanol (IPA, 99.7 %, BDH) was added with rapid mixing to a water-IPA solution to give a final molar composition of 1 TIP: 24 IPA: 5 H_2O. Amorphous titania gel spheres of uniform size and shape were formed during the rapid hydrolysis of the titanium alkoxide precursor. The suspension was aged for an hour before filtration. Nanostructured TiO_2 of different crystal sizes (i.e., 9A, 13A, 18A and 23A) were crystallized

Table 1

Physicochemical properties of TiO_2 support

TiO_2 support	Thermal treatment condition	Crystal phase	TiO_2 crystal size[a] (nm)	BET area (m^2/g)	Average pore diameter[c] (nm)	Pore volume (cm^3g^{-1})
P25	-	18% Anatase[b] 82% Rutile	24 (Anatase) 31 (Rutile)	54 ± 2	11.3	0.16
18A	Calcined at 823 K for 15 min in air	Anatase	18	48 ± 1	5.4	0.13
18R	Microwave in 1M HCl for 1 h	Rutile	18	46 ± 1	7.1	0.30
9A	Calcined at 693 K for 1 h in air	Anatase	9	150 ± 5	2.9	0.21
13A	Calcined at 693 K for 3 h in air	Anatase	13	80 ± 2	3.4	0.17
23A	Calcined at 823 K for 1 h in air	Anatase	23	20 ± 1	7.1	0.08
9M	Microwave in 1M H_2SO_4 for 30 min	Anatase	9	188 ± 6	1.2	0.12
UV100	-	Anatase	9	324 ±10	2.4	0.38

[a]calculated from XRD peak broadening of anatase TiO_2 (101) and rutile (110).
[b]calculated from the XRD peak intensity using the formula of

$$W_A = \left(\frac{k_A A_A}{k_A A_A + A_R} \right) \quad \& \quad W_R = \left(\frac{A_A}{k_A A_A + A_R} \right)$$

where W is the weight fraction of phase, $k_A = 0.884$, A_A is the integrated intensity of anatse (101) and A_R is the integrated intensity of rutile (110) (31).
[c]calculated by average pore diameter = 2(total pore volume)/BET surface area for slit shape pores.

from the amorphous gel spheres by air calcinations in a high temperature furnace (Carbolite BOF 11/13). A 9 nm anatase TiO_2 (i.e., 9M) was prepared by microwave-assisted hydrothermal treatment of the amorphous titania gel spheres in a concentrated sulphuric acid solution, while a rutile TiO_2 (i.e., 18R) was crystallized using a similar procedure from a hydrochloric acid solution (26-30). Also, a commercial anatase TiO_2 Hombikat UV100 was purchased from Sachtleben. The preparation conditions and physicochemical properties of the TiO_2 supports are summarized in Table 1.

The gold was deposited onto the TiO_2 supports at a neutral pH from a gold chloride solution. 1 g of TiO_2 powder was suspended in double distilled, deionised (DDI) water and 20 mL of 2.5 mM hydrogen tetrachloroaurate (III) trihydrate (Aldrich, A.C.S. reagent) solution were added. The pH was adjusted by adding Na_2CO_3 (BDH, 99.9%) and the resulting suspension was stirred in the dark at room temperature for half an hour. The catalyst was filtered and washed with hot water (i.e., 368 K), before drying in a vacuum oven at 298 K for 24 h. The gold catalyst was pre-treated in ozone (100 ppm O_3/O_2) at 473 K for 5 h. The ozone was generated from high purity oxygen gas (99.7 %) by an electrical discharge ozone generator (Trailigaz, Ozoconcept OZC100). An ozone gas analyser (Trailigaz, Uvozon TLG 200) monitors the ozone feed concentration entering the pre-treatment cell. The gold catalysts were reduced *in situ* during the CO oxidation reaction.

2.2 Characterization of Au/TiO_2 Catalysts

The TiO_2 supports and gold catalysts were characterized by different techniques including X-ray diffraction (XRD, Philips PW1830) and micro-Raman spectroscopy (Renishaw) to determine the support phase structure, crystal size and crystallinity. X-ray diffraction data were collected between $20^o < 2\Theta < 65^o$ at a scan rate of 0.05^o. The XRD was equipped with a CuKα X-ray source and a graphite monochromator. The gold catalyst was coated on a glass slide and analysed by Renishaw RM series Raman microscope using a 20 mW Argon laser (514.5 nm). The signals between 50 and 1000 cm^{-1} were collected at a resolution of 1.5 cm^{-1}. The textural properties of the TiO_2 including the specific surface area, pore size and pore volume were determined by nitrogen physisorption (Coulter SA 3100) after outgassing in vacuum for two hours at 393 K.

The catalyst gold loading was measured by inductively coupled plasma atomic emission spectroscopy (ICP-AES, Perkin Elmer Optima 3000XL) after dissolving a sample of the catalyst. X-ray photoelectron spectroscopy (XPS, Physical Electronics PHI 5600) provided information on the surface elemental composition of the catalyst. The XPS used a monochromatic aluminum X-ray source at a shallow, grazing angle giving a sampling depth of less than 1 nm. The gold particle size distribution was obtained by measuring more than a hundred individual gold particles imaged by high-resolution transmission electron microscopy (HRTEM, JEOL JEM 2010). The average gold particle size of the catalyst was calculated from equation 1.

$$\bar{d} = \frac{\sum n_i d_i}{\sum n_i} \qquad \text{Eqn. 1}$$

where n_i is the number of particles with a diameter d_i.

Table 2
Physicochemical properties of gold catalysts.

Catalyst	Au loading[a] (wt. %)	Average. coverage (Au atom nm^{-2})	Au particle size[b] (nm)	R_0[c] (mmol $s^{-1}g_{Au}^{-1}$)
GRC-A	1.41	0.80	2.05 ± 0.08	0.0721
Au18A	0.52	0.33	1.49 ± 0.07	0.1356
Au18R	1.10	0.73	2.38 ± 0.32	0.0130
Au9A	0.74	0.15	2.52 ± 0.24	0.0941
Au13A	0.71	0.27	1.69 ± 0.12	0.1049
Au23A	0.26	0.40	1.85 ± 0.19	0.2827
Au9M	0.67	0.11	1.40 ± 0.08	0.0356
AuUV100	0.61	0.06	1.66 ± 0.25	0.1498

[a]measured by ICP-AES after acid digestion.
[b]mean particle size measured by TEM.
[c]initial CO reaction rate for $[CO]_{Air}$ = 248 ppm, Q = 200 sccm and 298 K.

2.3 CO Oxidation Reaction on Au/TiO_2 Catalysts

The catalytic oxidation of carbon monoxide on Au/TiO_2 catalysts was carried out in the Operando-DRIFTS (diffuse reflectance infrared Fourier transformed spectroscopy) cell equipped with on-line CO gas analyzer and gas chromatography (32). The reactor setup consists of a gas delivery system, a DRIFTS reactor cell from Harrick, a Perkin Elmer FTIR spectrometer (GX 2000), a Horiba VIA-510 CO gas analyser and a Hewlett Packard gas chromatograph (HP 6890) equipped with thermal conductivity and flame ionisation detectors. The catalyst was packed in a heated receptacle inside the DRIFTS reactor cell specially designed to minimize reflection losses from the windows and maximize the light interaction with the sample. The reactor cell was placed in the Harrick diffuse reflectance attachment unit inside the FTIR spectrometer. The praying mantis mirror arrangement directs the incident IR beam onto the surface of the catalyst bed and collects the diffuse reflectance for analysis by the FTIR spectrometer. Each spectrum is an average of sixty-four scans at 0.5 cm^{-1} resolution obtained from 500 to 4000 cm^{-1} with an optical path difference velocity of 2 cms^{-1}.

30 mg of gold catalyst was used for each reaction. The catalyst was purged with dry synthetic air at room temperature for an hour before reaction. The carbon monoxide (248 ppm) and dry synthetic air (22% O_2 and 78% N_2) were metered by electronic mass flow controllers (Sierra 810S-Series Mass-Trak) and mixed before entering the reactor cell. The feed flowrate was maintained at 200 sccm (i.e., standard cm^3min^{-1}) to give a space velocity of 132,000 h^{-1}. The CO oxidation reaction was carried out at room temperature and surface reaction was monitored by DRIFTS, while the exit gas was analysed by CO gas analyser and gas chromatograph to determine the reaction conversion and selectivity.

3 Results and discussion

3.1 WGC's Gold Reference Catalyst (GRC-A)

The gold reference catalyst (GRC-A, 1.47 wt. % Au/TiO_2) supplied by the World Gold Council was characterized and tested for CO oxidation reaction. The X-ray diffraction pattern of GRC-A shown in Figure 1a display the diffraction peaks for TiO_2 anatase and rutile crystal phases belonging to the support material. The XRD was unable to detect the diffraction peaks from the gold catalyst particles, which is a good indication of a well- dispersed catalyst. The XRD pattern of the GRC-A was very similar to the commercial Degussa P25 TiO_2 that it can be safely inferred to be the support material used in the preparation of GRC-A. It can be estimated from the XRD data that the support consisted roughly of 18 wt. % rutile and 82 wt. % anatase TiO_2. The rutile and anatase TiO_2 measured 31 and 24 nm, respectively. Analysis of the catalyst by micro-Raman (Figure 1b) confirmed the presence of mixed phase TiO_2. The nitrogen adsorption and desorption isotherms for the catalyst shown in Figure 1c displays a type II isotherm with a type H4 hysteresis. The type-II isotherm is a characteristic of multilayer adsorption on nonporous or macroporous solids and the type-H4 hysteresis is often associated with slit shape microporosity (33). The catalyst has a surface area of 54 ± 2 m^2/g and a pore volume of 0.16 cm^3/g similar to that of the Degussa P25 TiO_2.

The GRC-A has a reported gold loading of 1.47 wt. %, which is close to the value of 1.41 wt. % determined experimentally by ICP-AES. The gold on GRC-A is present as reduced metallic Au^0 according to the results of X-ray photoelectron spectroscopy (34) shown in Figure 2a. The Au4f binding energies of the GRC-A are 83.5 and 87.3 eV. XPS also detected carbon (C/Ti = 0.058) and chlorine (Cl/Ti = 0.003) on fresh GRC-A. Figure 3a displays a high-resolution transmission electron micrograph of the fresh GRC-A catalyst. It can be seen from the micrograph that the gold catalyst particles are evenly distributed on the rutile and anatase TiO_2

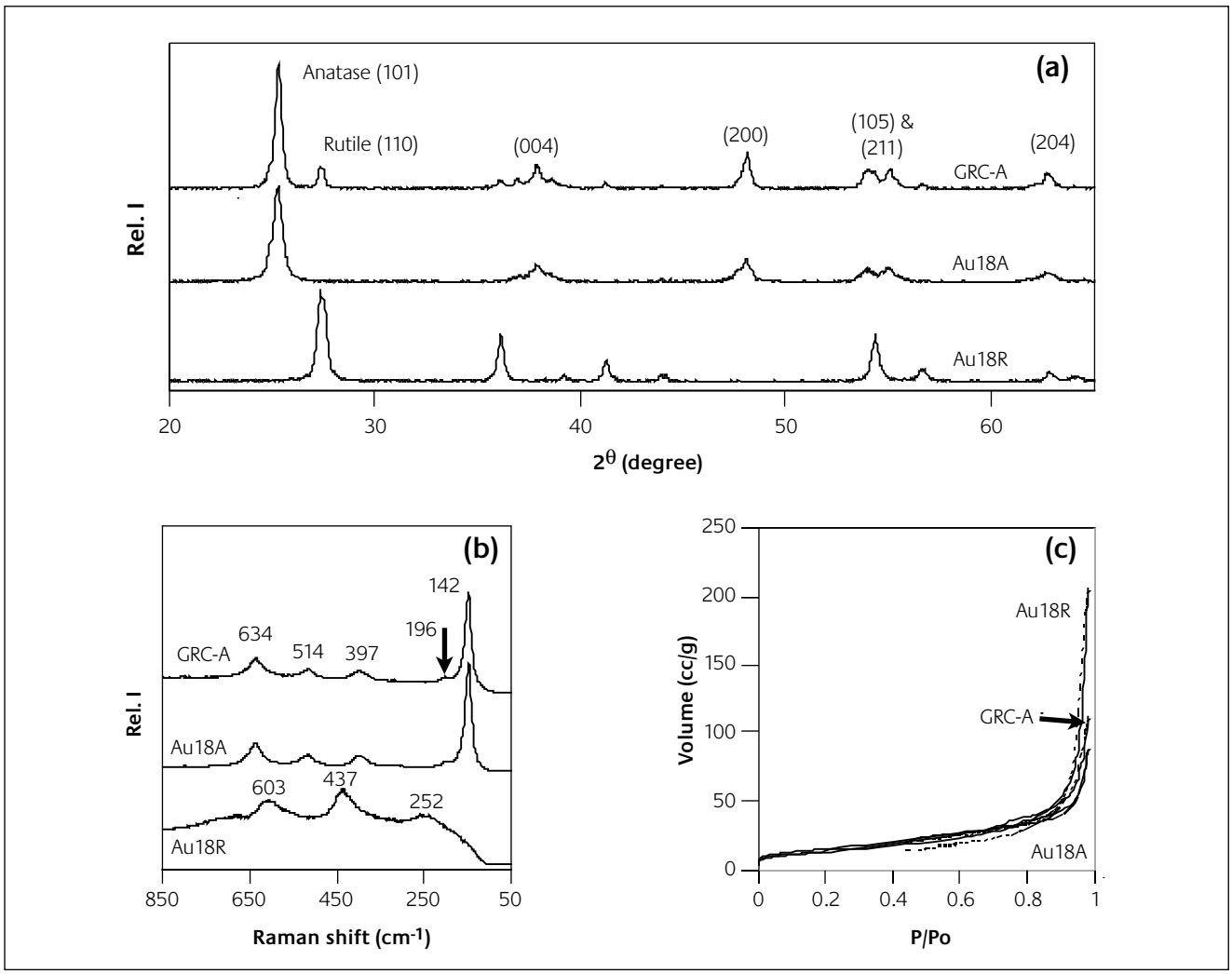

Figure 1

(a) X-ray diffraction, (b) micro-Raman spectra and (c) N_2 adsorption-desorption isotherms for GRC-A, Au18A and Au18R catalysts.

crystals. The gold particle size distribution exhibits a typical Gaussian distribution (Figure 4a) with an average gold particle size of 1.5 nm.

The GRC-A catalyst was used for room temperature CO oxidation reaction without additional pre-treatment. The CO oxidation reaction was carried out in the Operando-DRIFTS cell equipped with on-line CO gas analyzer and gas chromatography. The reaction was conducted in the DRIFTS reactor cell at 298 K with a flowing reactant mixture of 248 ppm CO in dry air at a space velocity of 132,000 h^{-1}. The surface reaction was monitored by infrared spectroscopy and the reaction conversion and selectivity were determined by the on-line CO gas analyzer and gas chromatography. Figure 5a plots the CO conversion rate over the GRC-A as a function of time. The initial CO conversion rate for the catalyst was 0.07 $mmol^1s^{-1}g_{Au}^{-1}$, but the catalyst deactivated to 0.05 $mmol^1s^{-1}g_{Au}^{-1}$ after five hours of reactions. The catalyst deactivation was investigated for a longer time and the results are plotted in Figure 6a. The GRC-A lost half of its activity during the first five hours of reaction with the CO conversion decreasing from 91 to 59%. At the end of the ten hours reaction, the catalyst conversion was about 50%.

The infrared spectra shown in Figure 5b were obtained at different time intervals during the reaction. Surface hydroxyls and adsorbed water were evident on the GRC-A catalyst even after 1 h of purging in dry air at room temperature. The infrared signals at 3690 and 3665 cm^{-1} belonging to the vibration of surface hydroxyls and the signal at 3634 cm^{-1} from the stretching of adsorbed water (35, 36) were observed, as well as the broad band at 1629 cm^{-1} is typically assigned to adsorbed water molecules. Surface dehydration occurred almost immediately after flowing in the reactant mixture. Infrared signals for adsorbed CO on gold surface at 2112 cm^{-1} (11), non-coordinated carbonate at 1430 cm^{-1} (2) and monodentate carbonate at 1360 and 1530 cm^{-1} (12) were detected during the reaction (Figure 5b-(i) to (vi)). It had been established by Haruta *et al.* (14) that the surface carbonates are deposited on the TiO_2 surface around the vicinity of the gold catalyst particles. The stronger carbonate signals suggest an accumulation of surface carbonate species as the reaction progresses. The surface carbonates could interfere with the reaction and could be the reason for the weaker CO signal at the longer reaction time as shown in Figure 5b-(v). The weaker CO signal signifies less CO adsorption on the catalyst surface. It is clear from the gold particle size distribution in Figure 4b that the catalyst suffered from sintering and loss

of active surface area despite the low reaction temperature. This could be due to the weak catalyst support interaction.

3.2. Effects of TiO_2 Crystal Phase Structure

The GRC-A catalyst was supported on a biphasic TiO_2 support (cf. Figure 1). Two TiO_2 supports, a pure anatase (18A) and a pure rutile (18R) TiO_2 were prepared in order to investigate the effects of TiO_2 crystal phase structure on the gold catalyst performance for CO oxidation reaction. The TiO_2 supports have comparable crystal size of 18 nm and specific surface area of about 50 m^2/g as shown in Table 1. The gold catalyst (Au18A) prepared from 18A displays only the X-ray diffraction peaks belonging to anatase TiO_2 as shown in Figure 1a. The figure also plots the diffraction data of Au18R prepared from the rutile TiO_2 support. The catalyst displays the characteristic XRD peaks for rutile TiO_2 (i.e., (110), (101), (111), (211)). The Raman spectra of Au18A and Au18R are shown in Figure 1b. The Au18A catalyst displays only the characteristic signals for

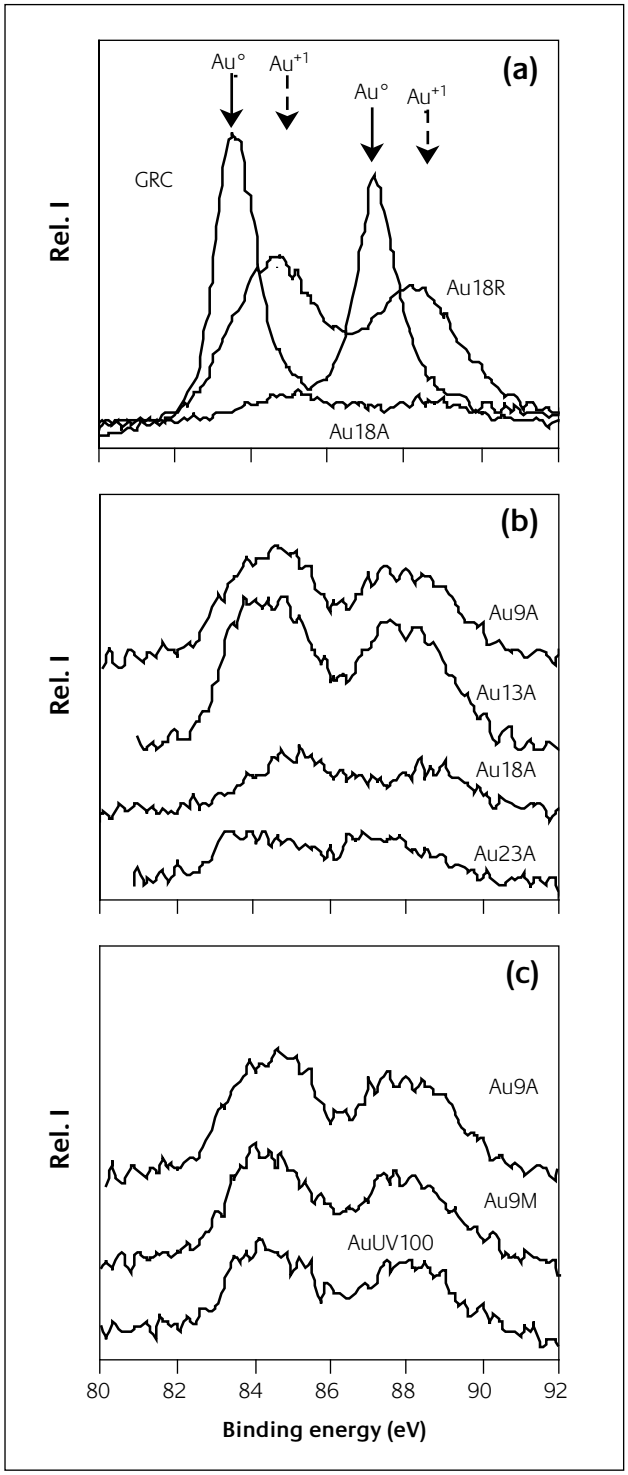

Figure 2

X-ray photoelectron spectra of Au_{4f} for gold catalysts prepared on TiO_2 with different (a) phase structure, (b) crystal size and (c) surface and textural properties.

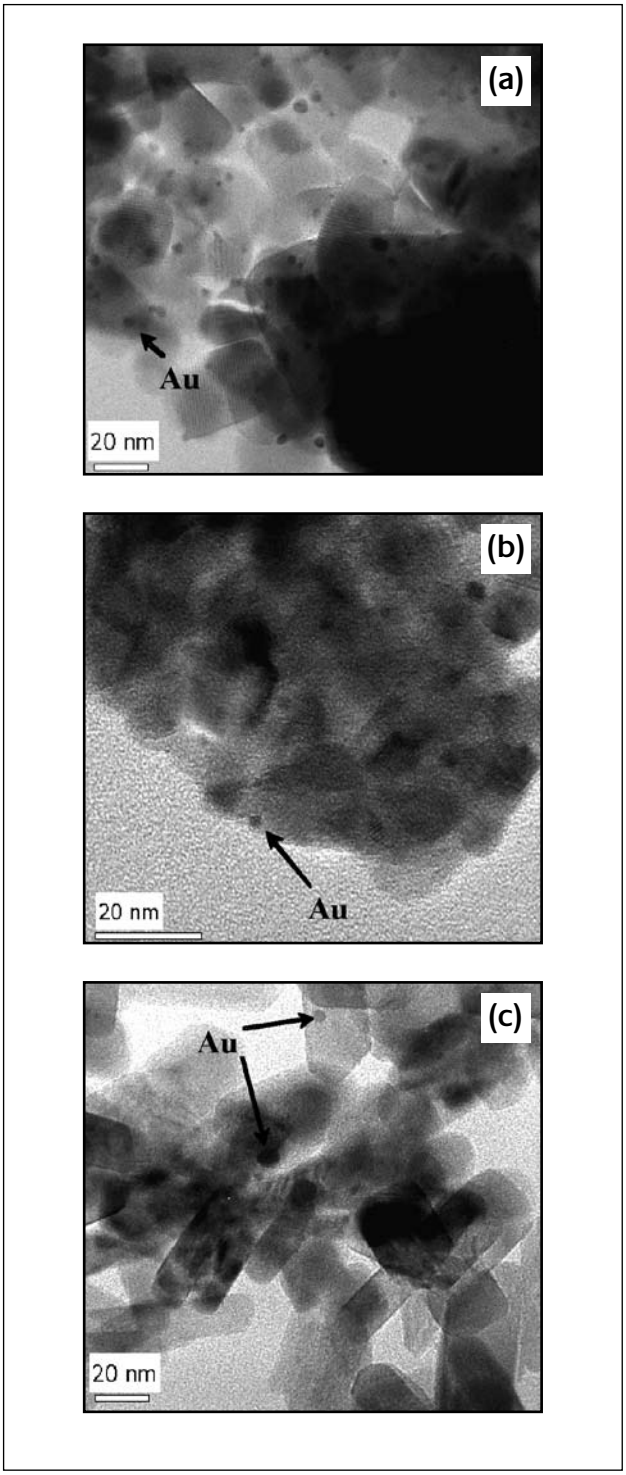

Figure 3

High-resolution transmission electron micrographs of fresh (a) GRC-A, (b) Au18A and (c) Au18R catalysts.

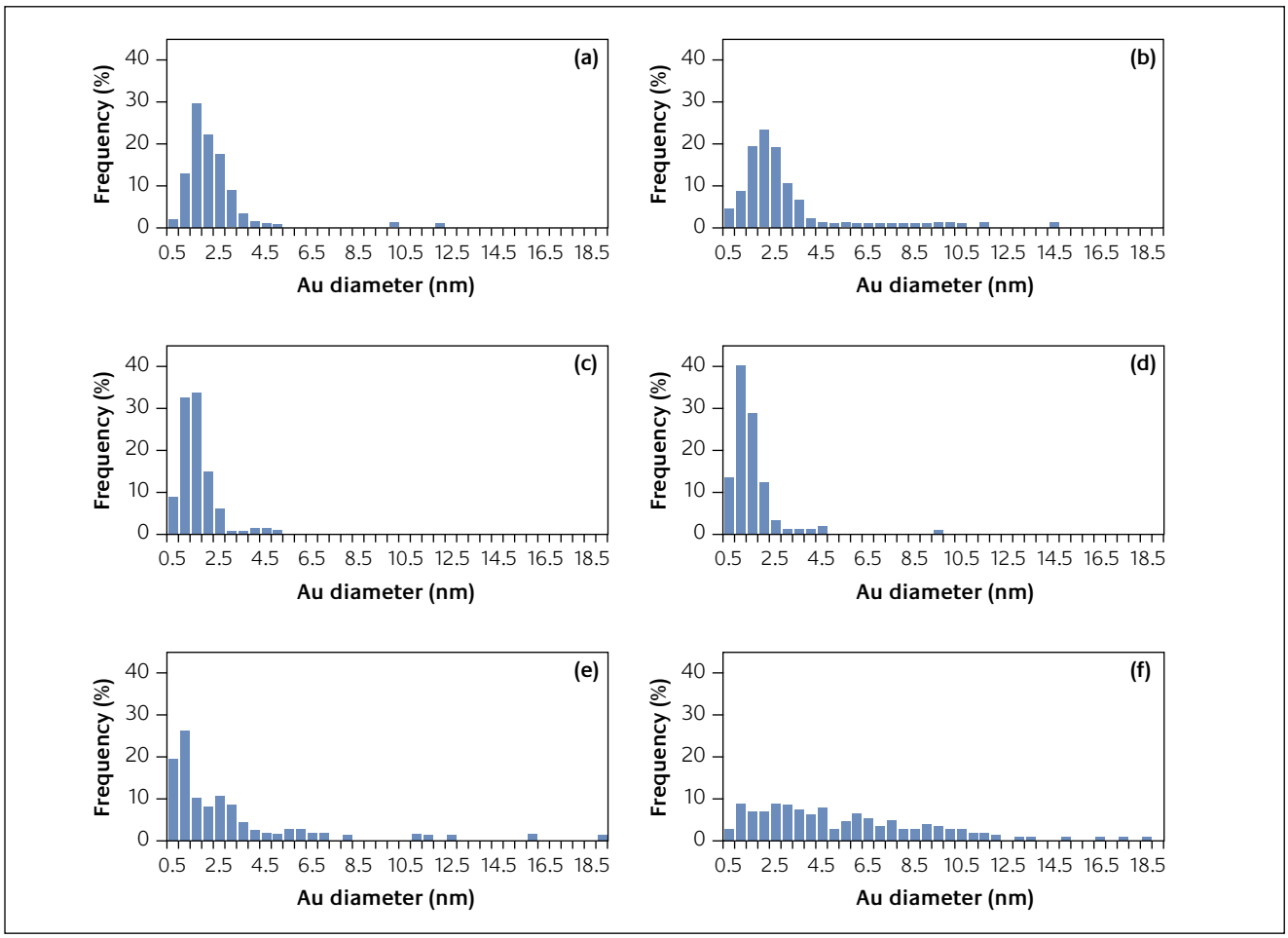

Figure 4

Gold particle size distributions of fresh and spent gold catalysts (a) & (b) GRC-A, (c) & (d) Au18A and (e) & (f) Au18R.

anatase TiO_2 including the 637, 196 and 146 cm^{-1} belonging to the E_g mode, the 516 cm^{-1} assigned to the doublet of A_{1g} and B_{1g} modes and 395 cm^{-1} corresponding to the B_{1g} mode (37). The Au18R shows only signals belonging to rutile TiO_2 at 603 cm^{-1} for A_{1g} mode, 437 cm^{-1} for E_g mode and the band at 252 cm^{-1} assigned to combination band (37).

Nitrogen physisorption experiments show that both Au18A and Au18R catalysts displays a type II isotherm with a type H4 hysteresis similar to the GRC-A catalyst as shown in Figure 1c. This means that besides having similar crystal size and surface area, all three catalysts also have similar pore structures and geometries and differ only in their pore volumes (Table 1). The Au18A and Au18R catalysts were prepared under identical conditions, but the final gold loading of Au18A (0.52 wt. %) was less than Au18R (1.1 wt. %). This could be due to the difference in the surface structure and chemistry of the anatase and rutile TiO_2. Previous work had established that ozone pretreatment of gold catalysts improves both catalyst reactivity and stability (32). Both Au18A and Au18R were pretreated with ozone and analysed by XPS. Figure 2a shows both catalysts have higher and broader Au_{4f} binding energies indicating the presence of oxidic gold. Although the rutile TiO_2 support (18R) was prepared by hydrothermal treatment in concentrated HCl solution, only a trace amount of chloride ions (< 0.1 at. %) was detected on the Au18R catalyst comparable to that found in the Au18A and GRC-A catalysts.

The TEM pictures of Au18A and Au18R are shown in Figures 3b and 3c, respectively. The gold on Au18A is highly dispersed and exhibits a narrow particles size distribution (Figure 4c). It can be seen from the micrograph in Figure 3b that the nanometer-sized gold particles are evenly distributed on the TiO_2 support. The figure also shows the 18 nm, quasi-spherical anatase TiO_2 are agglomerated into clusters of 100 nm. In contrast to the irregular shape of the anatase TiO_2 in Au18A, the rutile TiO_2 of Au18R has the shape of an elongated prism as shown in Figure 3c. The rutile TiO_2 crystals are roughly 20 nm in width and 50 nm in length. The gold deposited on Au18R has a broader particle size distribution (Figure 4e) and it is not uncommon to see gold particles with diameter larger than 10 nm.

The CO oxidation reaction was conducted using operando-DRIFTS and the results are shown in Figure 5. The CO conversion rates for the Au18A and Au18R catalysts are plotted against reaction time in Figure 5a. The Au18A performs better than the GRC-A catalyst, while Au18R displays the worst CO conversion rates among the three catalysts as shown in the figure. It can be seen in Figure 6a that the initial CO conversion on Au18A is high despite containing less than a third of gold loading used in GRC-A. On the other hand,

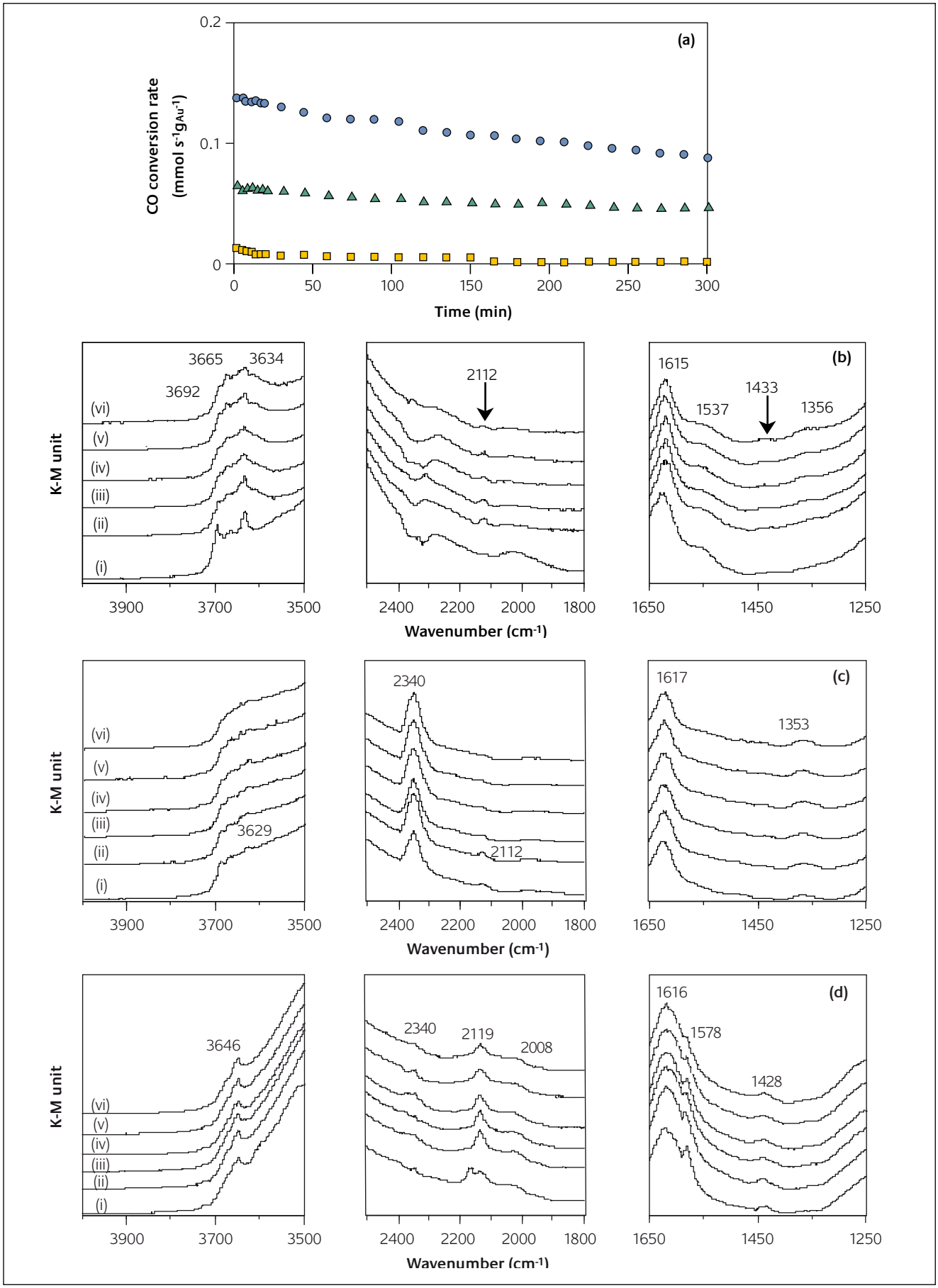

Figure 5

Operando-DRIFTS study of CO reaction on GRC-A, Au18A and Au18R catalysts. (a) CO conversion rates versus time for GRC-A (△), Au18A (O) and Au18R (□) and DRIFTS spectra of CO reaction on (b) GRC-A, (c) Au18A and (d) Au18R after reaction of 1 min (i), 60 min (ii), 120 min (iii), 180 min (iv), 240 min (v) and 300 min (vi).

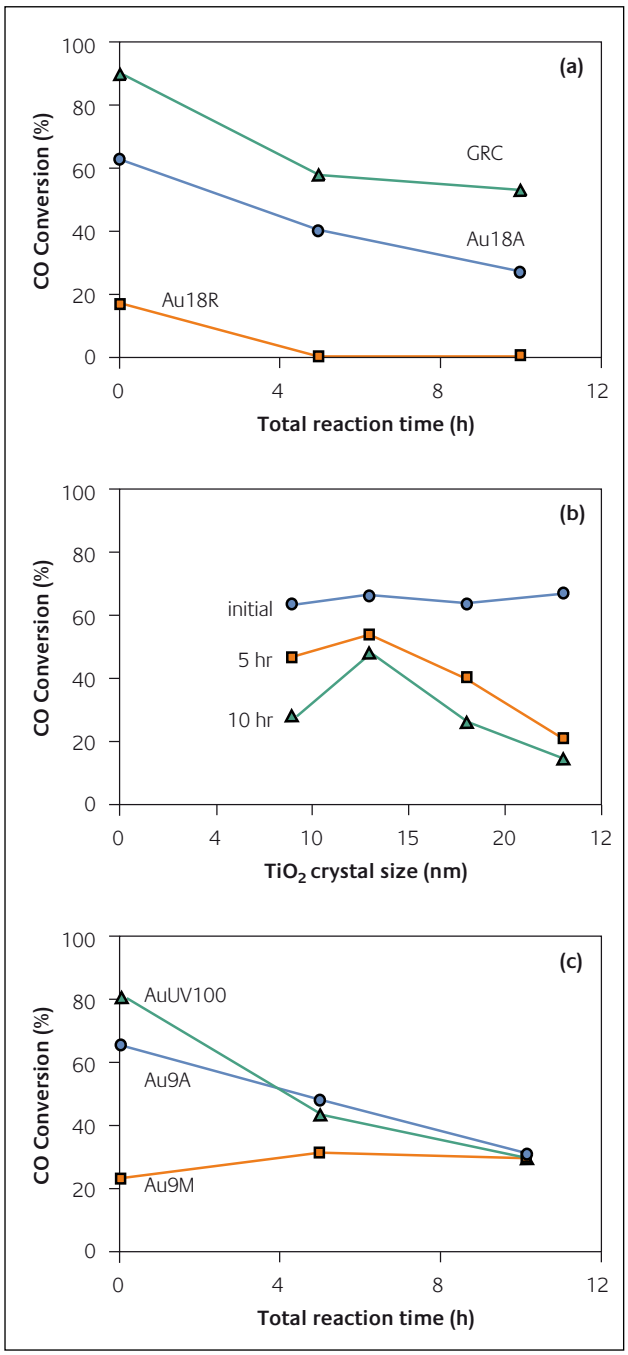

Figure 6

CO conversion as a function of time for gold catalysts prepared on TiO_2 with different (a) phase structure, (b) crystal size and (c) surface and textural properties.

the Au18R catalyst was unable to even maintain the low CO conversion of 17 % for more than half an hour.

The surface reactions on the Au18A and Au18R were monitored with time and the DRIFT spectra are shown in Figures 5c and 5d, respectively. Surface hydroxyls and adsorbed water were present on the gold catalysts even after an hour of dry air purging of Au18A and Au18R. Both gold catalysts had a strong signal at 1620 cm^{-1} from adsorbed water. The Au18A displayed infrared bands belonging to the surface hydroxyls (i.e., 3693 and 3668 cm^{-1}) (35, 36) and adsorbed water (i.e., 3630 cm^{-1}) (38). The Au18R had infrared bands at 3690 and 3650 cm^{-1} belonging to the isolated hydroxyls and bridged hydroxyls (35). Au18R also showed infrared signals at 1578 and 1227 cm^{-1} that were assigned to bidentate carbonates (39, 40). It was clear from the spectra that the surface hydroxyls on anatase (i.e. 3693 and 3668 cm^{-1}) and rutile (i.e. 3690 and 3650 cm^{-1}) TiO_2 were different. A closer examination of GRC-A detected the presence of both types of surface hydroxyls from the anatase and rutile TiO_2.

Dehydration is evident in Au18A with the disappearance of of 3693, 3668 and 3630 cm^{-1} bands (Figure 5c-(i) to (vi)). This was not observed in the Au18R where the band belonging to isolated hydroxyl group at 3690 and bonded hydroyl groups at 3650 cm^{-1} remained unchanged during the entire five hours of reaction. Also, there was a significant build-up of monodentate carbonate (1350 cm^{-1}) on Au18A (Figure 5c-(i) to (vi)) that was not observed on Au18R. Instead, non-coordinated carbonates (1428 cm^{-1}) are prevalent in the latter catalyst as shown in Figure 5d-(i) to (vi)). The gold particle size distribution of Au18A remained relatively unchanged after the reaction (Figure 4d), but the Au18R suffered a dramatic change caused by sintering as shown in Figure 4f.

It can be clearly seen from the experimental results that catalyst activity and life are strongly affected by the support material. The Au18R supported on rutile TiO_2 had the lowest activity and shortest life among the three catalysts. Although the recent work of Moreau and Bond (20) reported exceptional performance for gold catalyst on rutile TiO_2, the catalytic activity of Au18R is more in accordance with earlier reports where gold on rutile TiO_2 often has poorer reaction performance. The Au18R also suffered from rapid deactivation caused by the sintering of the gold catalyst. The main reason is the poor catalyst support interaction. Indeed, the work of Valden and Goodman (3) showed that 2-3 nm gold particles on rutile TiO_2 were very mobile and tended to aggregate upon exposure to O_2 gas and CO/O_2 mixture at room temperature (i.e., 300 K). The GRC-A on biphasic TiO_2 support (18 wt. % rutile & 82 wt. % anatase) performed significantly better than Au18R, but suffered from deactivation caused by gold sintering and surface carbonate deposition. It is interesting to note that monodentate carbonate found on Au18A (i.e., anatase TiO_2) and the non-coordinated carbonate that is prevalent on Au18R (i.e., rutile TiO_2), are present on the GRC-A (i.e., biphasic TiO_2). The Au18A prepared on pure anatase TiO_2 performed the best among the three catalysts. It maintained a high CO conversion rate compared to both Au18R and GRC-A. Gold sintering was not observed, but the catalyst deactivated due to the deposition of monodentate surface carbonates. The catalyst deactivation is therefore reversible and a simple heating to 623 K can regenerate the catalyst activity.

3.3. Effects of Anatase TiO_2 Particle Size

It has been established in the last section that anatase TiO_2 is a better support than either rutile TiO_2 or biphasic TiO_2. Anatase TiO_2 supports of different crystal sizes were prepared by the modified sol-gel method (21). The colloidal titania gel spheres were formed by the rapid hydrolysis of

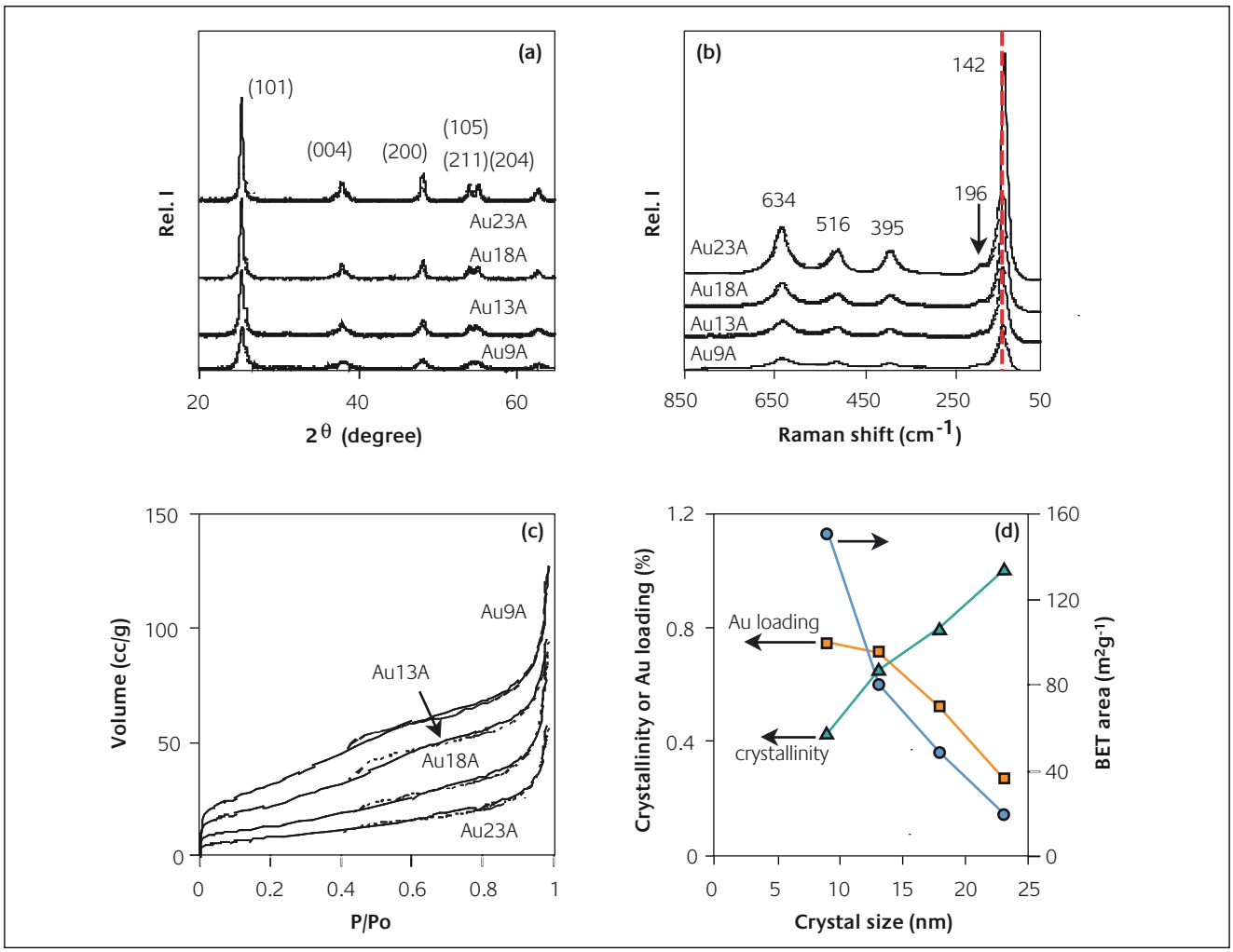

Figure 7

(a) X-ray diffraction, (b) micro-Raman spectra and (c) N_2 adsorption-desorption isotherms for gold catalysts supported on TiO_2 of different crystal sizes (i.e., Au9A, Au13A, Au18A and Au23A) and (d) plots of surface area, crystallinity and gold loading as a function of TiO_2 crystal size.

titanium isopropoxide solution in a water-isopropanol mixture. A vigorous mixing produces uniform gel spheres of about 100 nm in diameter. The dried gel spheres were calcined in air at elevated temperatures to crystallize the anatase TiO_2 (Table 1). Figure 7a displays the X-ray diffraction patterns of Au/TiO_2 catalysts, Au9A, Au13A, Au18A and Au23A prepared from anatase TiO_2 supports with crystal size of 9, 13, 18 and 23 nm, respectively. The particle size of the TiO_2 supports was determined from the X-ray diffraction line broadening of the anatase TiO_2 (101) peak. The XRD patterns of the gold catalysts shown in Figure 7a display only the characteristic diffraction peaks of anatase TiO_2 belonging to the support. The gold diffraction peaks were not detected and this could be due to the low gold loadings and the small size of the gold catalyst particles.

The gold catalysts were also analyzed by micro-Raman spectroscopy and the results are shown in Figure 7b. Raman spectroscopy is considered to be a more sensitive technique than XRD and could detect minute quantities of brookite and rutile crystal phases. The Raman spectra of all four gold catalysts display only the characteristic signals for anatase TiO_2. The Raman bands for the brookite and rutile TiO_2 crystal phases are absent from the spectra indicating that pure anatase TiO_2 supports were successfully prepared. Figure 7b shows the TiO_2 supports with small crystal size have weaker Raman signal due to the greater number of local lattice imperfections (41). A longer crystallization time and higher treatment temperature led to better TiO_2 crystallinity as indicated by the stronger diffraction peak signals and more intense Raman bands in Figures 7a & 7b, respectively. A red shift in the Raman peak from 149 to 146 cm^{-1} with increasing TiO_2 crystal size, is consistent with the reports of Lottici *et al.* (37) and Barborini *et al.* (42). Bersani and coworkers (43) attributed the observed peak shift and broadening to phonon confinement. However, defects and amorphous oxides are also known to cause Raman peak broadening. A comparison of the Raman spectra between the gold catalyst and the TiO_2 support showed a large decrease in the Raman signal after catalyst preparation. Also, a weak E_g peak at 196 cm^{-1} appeared after gold addition.

Nitrogen physisorption measurements were carried out to determine the textural properties of the gold catalysts. Figure 7c shows all four gold catalysts display a type II isotherm with a type H4 hysteresis that is typical of a predominantly

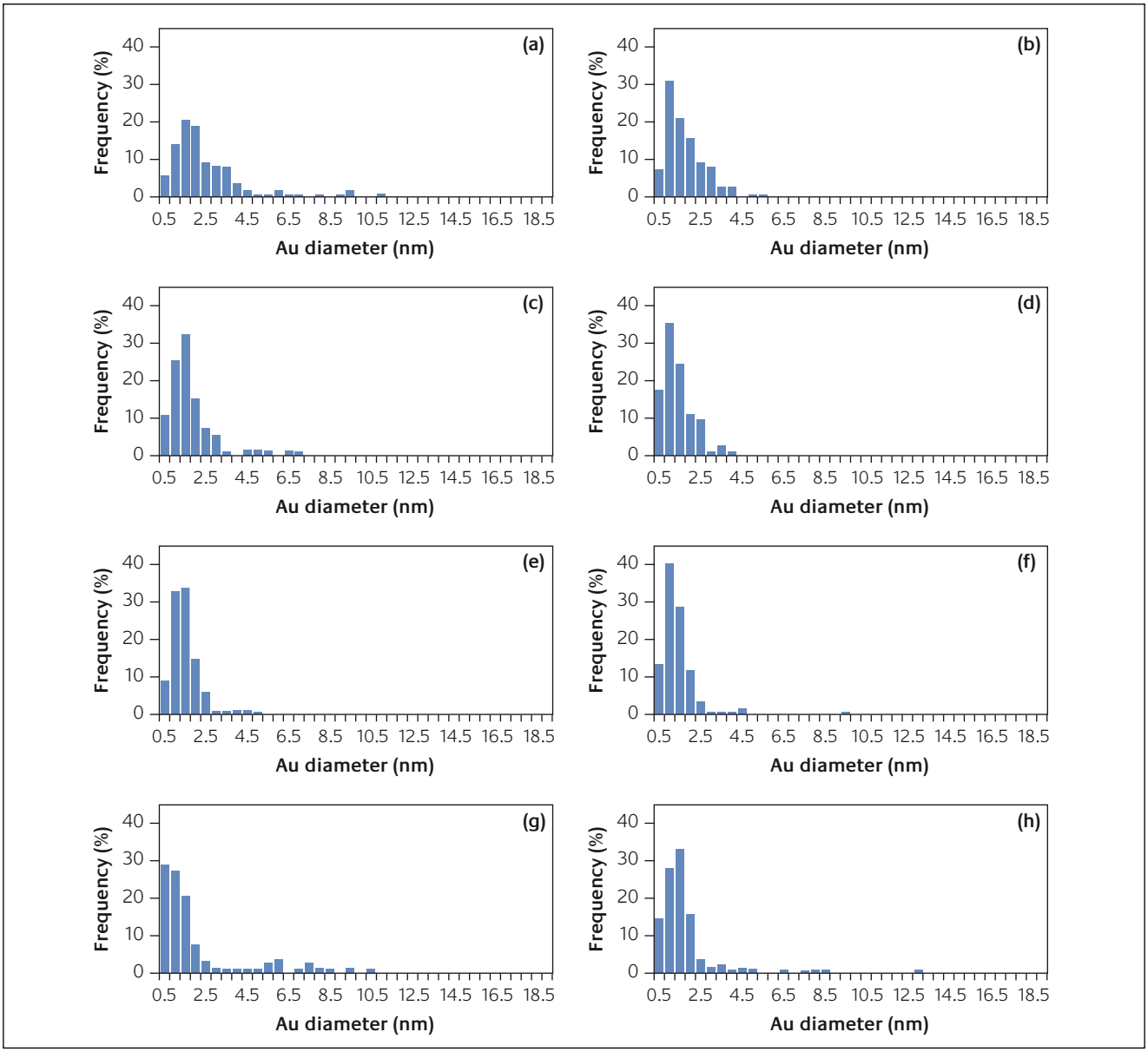

Figure 8

Gold particle size distributions of fresh and spent gold catalysts (a) & (b) Au9A, (c) & (d) Au13A, (e) & (f) Au18A and (g) & (h) Au23A.

macroporous solid containing slit-shaped pores (33). This suggests that the four catalysts have similar pore geometry despite the difference in the support particle size. On the other hand, the specific surface area and pore volume of the catalysts are smaller for those supported on TiO_2 with larger crystal sizes as shown in Table 1. The gold catalyst loading as measured by ICP-AES also shows a decreasing trend (Table 2). A recent work of Moreau and Bond (20) reported higher gold uptake for supports with larger surface area. Indeed, Au9A prepared from TiO_2 crystallized at a lower temperature possesses large surface area and abundant surface hydroxyls, also have the highest gold loading among the four catalysts. Figure 7d summarizes the effects of TiO_2 crystal size on the catalyst crystallinity, surface area and gold coverage. The crystallinity was estimated from the intensity of the XRD anatase (101) peak using Au23A as the reference.

Oxidation-reduction pre-treatment process is an established method for preparing well-dispersed metal supported catalysts (44-49). The gold catalysts were pre-treated in 100 ppm O_3/O_2 mixture at 473 K according to the procedure described in a recent work (32). The XPS data in Figure 2b clearly shows that oxidic gold are present on all the catalyst samples. The Au_{4f} peaks are broad and are positioned at a higher binding energy compared to the gold metal (34). The peak intensity is dependent on the gold loading and particle size (i.e., overall gold surface area). Study showed that properly stored gold catalysts treated by ozone showed oxidic gold under XPS even after a month in storage. However, the oxidic gold is readily reduced even in ambient air and should be handled carefully. The ozone-treated gold catalyst was reduced to metallic gold *in-situ* using the CO/air reaction mixture to produce a catalyst with improved activity and stability (32). The gold particle size distributions shown in Figures 8a-8h were obtained from the TEM pictures of the fresh gold catalysts. Gold catalysts supported on high surface area TiO_2 (i.e., Au9A and Au13A) display Gaussian particle

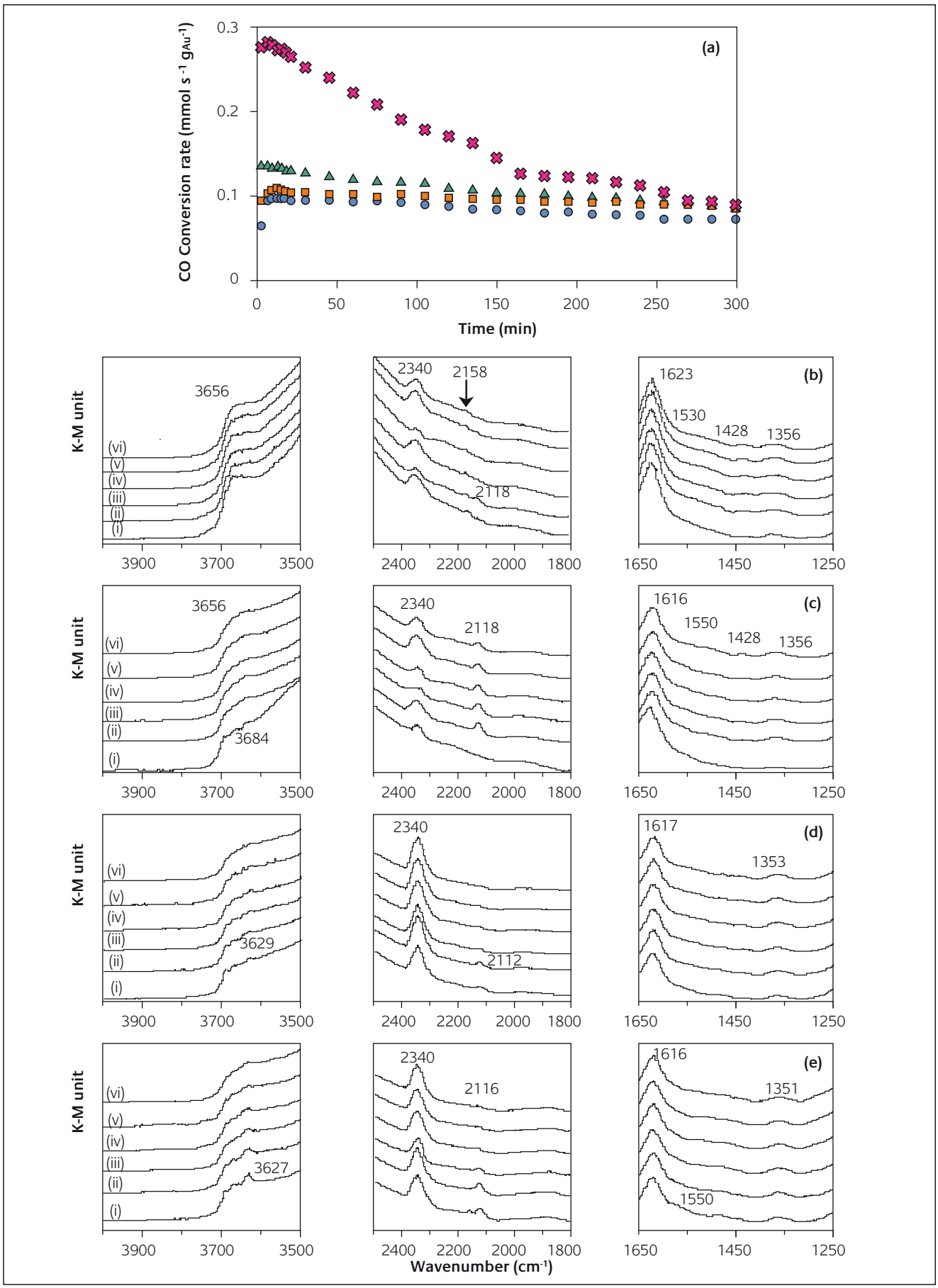

Figure 9

Operando-DRIFTS study of CO reaction on gold catalysts supported on TiO_2 of different crystal sizes (i.e., Au9A, Au13A, Au18A and Au23A). (a) CO conversion rates versus time for Au9A (●), Au13A (■), Au18A (▲) and Au23A (✖) and DRIFTS spectra of CO reaction on (b) Au9A, (c) Au13A, (d) Au18A and (e) Au23A after reaction of 1 min (i), 60 min (ii), 120 min (iii), 180 min (iv), 240 min (v) and 300 min (vi).

size distribution as shown in the figures, while a bimodal gold particle size distribution is evident in the Au18A and Au23A catalysts. It is important to note that the TEM measurement tends to overestimate the size of the particles. It is therefore more accurate to estimate the active gold catalyst area based on both XPS and TEM data, where Au13A > Au9A > Au18A > Au23A.

Figure 9a plots the CO conversion rates of the catalysts during five hours of reaction at room temperature. The reaction was carried out in the operando-DRIFTS reactor cell that permits the simultaneous monitoring of the surface reactions (Figures 9b-9e). The ozone-treated gold catalysts were reduced *in-situ* by the CO/air reactant mixture. Figure 6b shows the initial CO conversions of the catalysts are similar despite the difference in gold catalyst loading. However, calculations showed that the actual gold surface area of the catalysts used in the reaction was comparable and varied between 20-30 cm^2. The reaction will also be insensitive to gold catalyst loading if perhaps only a fraction of the gold catalyst participated in the reaction. This behaviour agrees with the reaction model proposed by Haruta *et al.* (14), where the CO oxidation reaction over Au/TiO_2 catalyst are believe to take place on a small number of gold atoms along the perimeter of the gold catalyst between CO adsorbed on the gold and O_2 adsorbed on the TiO_2. The reaction data in Figures 9a and 6b record the deactivation behavior of the gold catalysts. All four gold catalysts supported on anatase TiO_2 deactivated less than the GRC-A. It is clear from Figure 6b that Au13A has the best stability against catalyst deactivation followed by Au9A and Au18A catalysts, with Au23A having the worst performance. Examining the gold particle size distribution of the spent catalysts in Figures 8g-8h shows an increase in the gold particle size of Au23A after the room temperature CO oxidation reaction. The other three catalysts show clear evidence of gold redispersion with the disappearance of large gold particles after the reaction.

Figures 9b-9e displays the DRIFT spectra obtained at different time intervals during the room temperature CO oxidation reaction in Figure 9a. The broad band centered around 3656 cm^{-1} from the surface hydroxyls and the infrared signals at 3200 and 1620 cm^{-1} from adsorbed water were present on all four catalysts even after an hour of dry air purging. The infrared signals for isolated hydroxyls (i.e., 3690 cm^{-1}) and bonded hydroxyls (i.e., 3630 cm^{-1}) were indistinct for Au9A, but were clearly present in the other three gold catalysts. The intensity of these peaks increases with the TiO_2 crystal size. The infrared signals for surface hydroxyls (i.e., 3650, 3690 and 3630 cm^{-1}) decreased immediately at the very start of the reaction (Figures 9b-(i) to 9e-(i)). The infrared band for CO adsorbed on gold at 2116 cm^{-1} is present on all four catalysts as shown in the figure. A weak signal at 2158 cm^{-1} that had been assigned to CO adsorbed on oxidic gold sites (12) is also evident. The CO signals diminished with time (Figures 9b-9e) as the reaction rate of the catalyst decreases (Figure 9a). The infrared band at 2340 cm^{-1} belongs to CO_2 adsorbed on the catalyst surface.

The study also revealed the build up of surface carbonate species including non-coordinated carbonate (ca. 1428 cm^{-1}) and monodentate carbonate (ca. 1356 & 1530 cm^{-1}) during the reaction. Monodentate carbonate was detected on all four catalysts, while non-coordinated carbonate was present on Au9A and Au13A. The better gold dispersion (Figures 2b & 8) and stability (Figure 6b) of Au13A compared to Au9A could be due to the difference in the surface

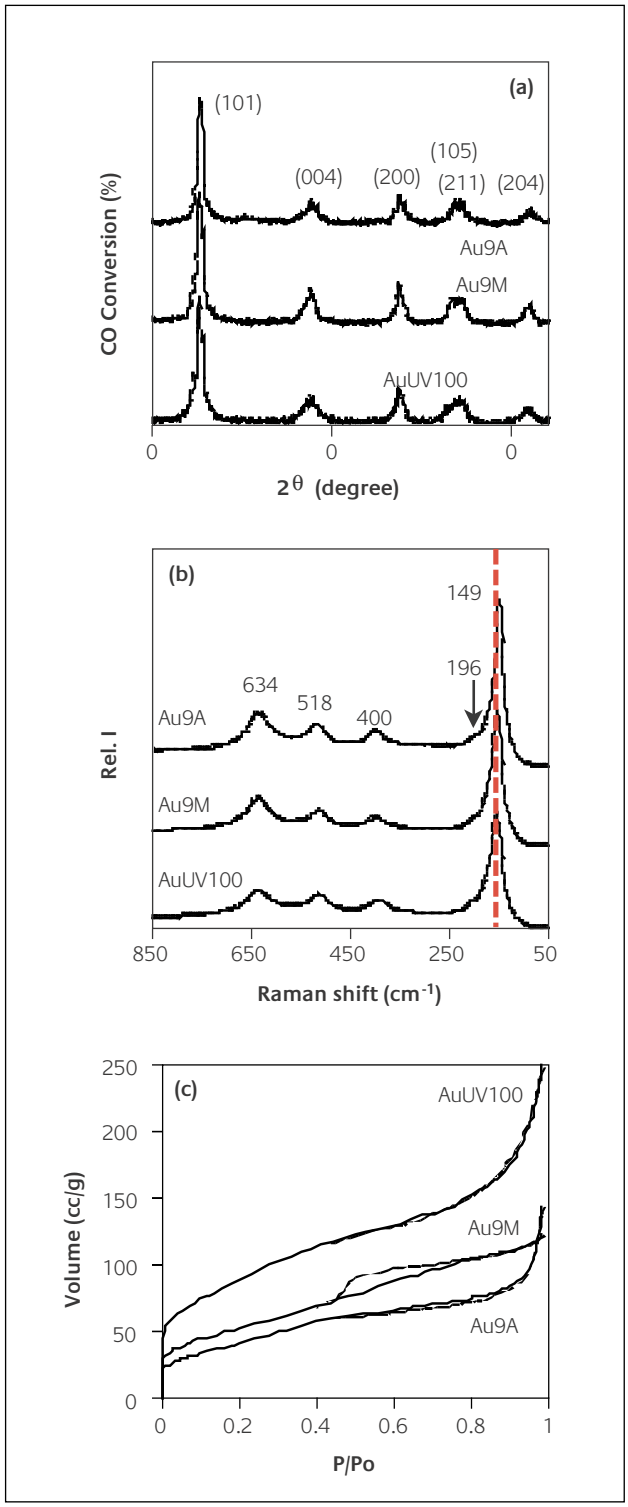

Figure 10

(a) X-ray diffraction, (b) micro-Raman spectra and (c) N_2 adsorption-desorption isotherms for Au9A, Au9M and AuUV100 gold catalysts.

(i.e., isolated and bonded hydroxyls) and textural properties (i.e., specific surface area and pore size) of TiO_2.

3.4. Effects of Surface and Textural Properties

The effects of TiO_2 surface and textural properties were further investigated. Two gold catalysts, Au9M and AuUV100 were prepared on TiO_2 supports of comparable crystal size. The 9M TiO_2 support was prepared by microwave-assisted hydrothermal treatment of titania gel spheres under concentrated sulphuric acid. FTIR and TGA/DTA analyses indicated that this support is roughly fifty percent more hydrated compared to the 9A TiO_2 prepared by air calcination. The other support was Hombikat UV100 bought from Sachtleben and was used without further pre-treatment. The 9M and UV100 supports are pure anatase TiO_2 of comparable crystal size and crystallinity to the 9A TiO_2 as shown by the XRD data in Figure 10a and micro-Raman spectra in Figure 10b. The nitrogen adsorption and desorption isotherms of Au9M in Figure 10c is a type II isotherm with a type H3 hysteresis normally found in aggregate clusters displaying irregular slit pores. It has the smallest pore size (i.e., 1.2 nm) and specific pore volume (0.12 cm^3g^{-1}) among the three catalysts and has a slightly larger surface area (188 ± 6 m^2g^{-1}) compared to Au9A (Table 1). The commercial UV100 has the largest specific surface area (i.e., 324 ± 10 m^2g^{-1}) and pore volume (i.e., 0.38 cm^3g^{-1}). Similar to Au9A, the nitrogen adsorption-desorption isotherm for AuUV100 is a type II isotherm with a type H4 hysteresis.

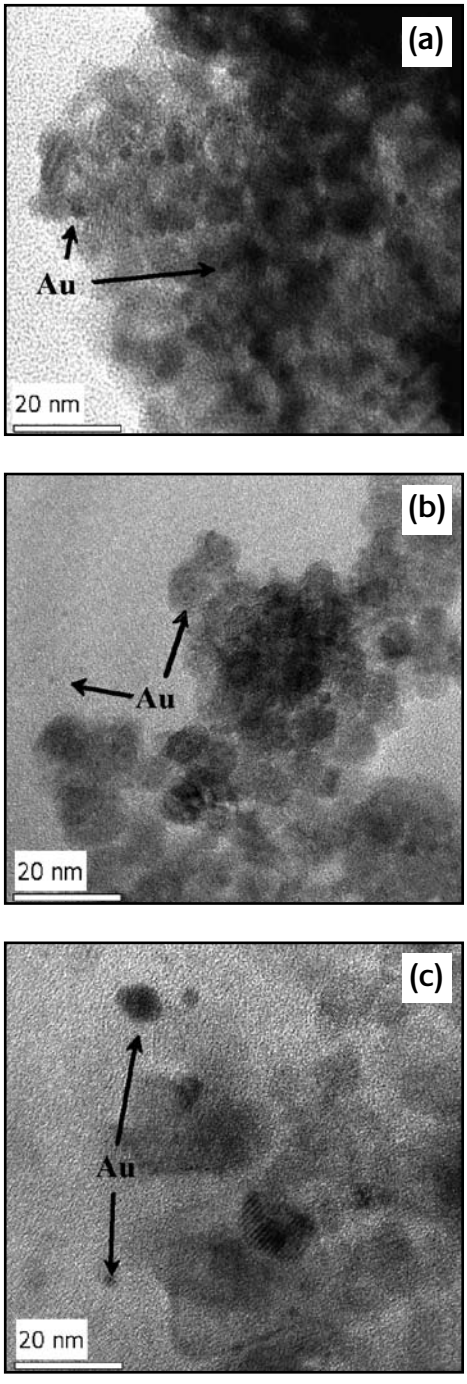

Figure 11

High-resolution transmission electron micrographs of fresh (a) Au9A, (b) Au9M and (c) AuUV100 catalysts.

The gold catalysts were prepared from the same precursor solution and under identical conditions on the three TiO_2 supports. Au9M and AuUV100 have similar gold loading as Au9A, in spite of 9M TiO_2 having a more hydrated surface and UV100 having twice the surface area. Oxidic gold were detected on both Au9M and AuUV100 after ozone treatment as shown by the higher Au_{4f} binding energies in Figure 2c. The transmission electron microscope pictures of the fresh Au9A, Au9M and AuUV100 are shown in Figure 11. The gold particles are uniformly dispersed on the 100 nm aggregate clusters of 9 nm 9A TiO_2 crystals as shown in Figure 11a. The gold particle size of Au9M has a mean value of 2.52 ± 0.24 nm. Figure 11b shows the TiO_2 in Au9M forms loose aggregate clusters of 9 nm-sized crystals. The gold deposited on the 9M TiO_2 have a mean particle size of 1.40 ± 0.08 nm (Table 1), but a large number of unsupported gold is observed in the sample (Figure 11b). The gold on AuUV100 is mostly located along the edges of the irregular shaped, TiO_2 aggregate clusters (Figure 11c). Gold particles larger than 10 nm are not uncommon for this catalyst, although the mean particle size is determined to be 1.66 ± 0.25 nm. The results show that gold dispersion displays a dependence on the pore size of the support. Gold is uniformly, well dispersed on 9A TiO_2 that has an average pore size of 2.9 nm, while the gold decorate the edges of the clusters in UV100 that has a pores of 2.4 nm and unsupported gold are common on 9M TiO_2 with 1.2 nm pores.

The Au9M catalyst has the lowest initial CO reaction rate compared to the other two catalysts (Figure 13a). This could be due to the large number of unsupported gold found on this catalyst. A slight activation was observed during the five hours of reaction and could be attributed to the catalyst redispersion shown in Figure 12d. The CO conversion for this catalyst is low but stable as shown in Figure 6c. The DRIFT spectra obtained during the reaction (Figure 13c) show the appearance of a peak at 1539 and 1323 cm^{-1} assigned to monodentate carbonate and a weak signal at 1430 cm^{-1} belonging to non-coordinated surface carbonates.

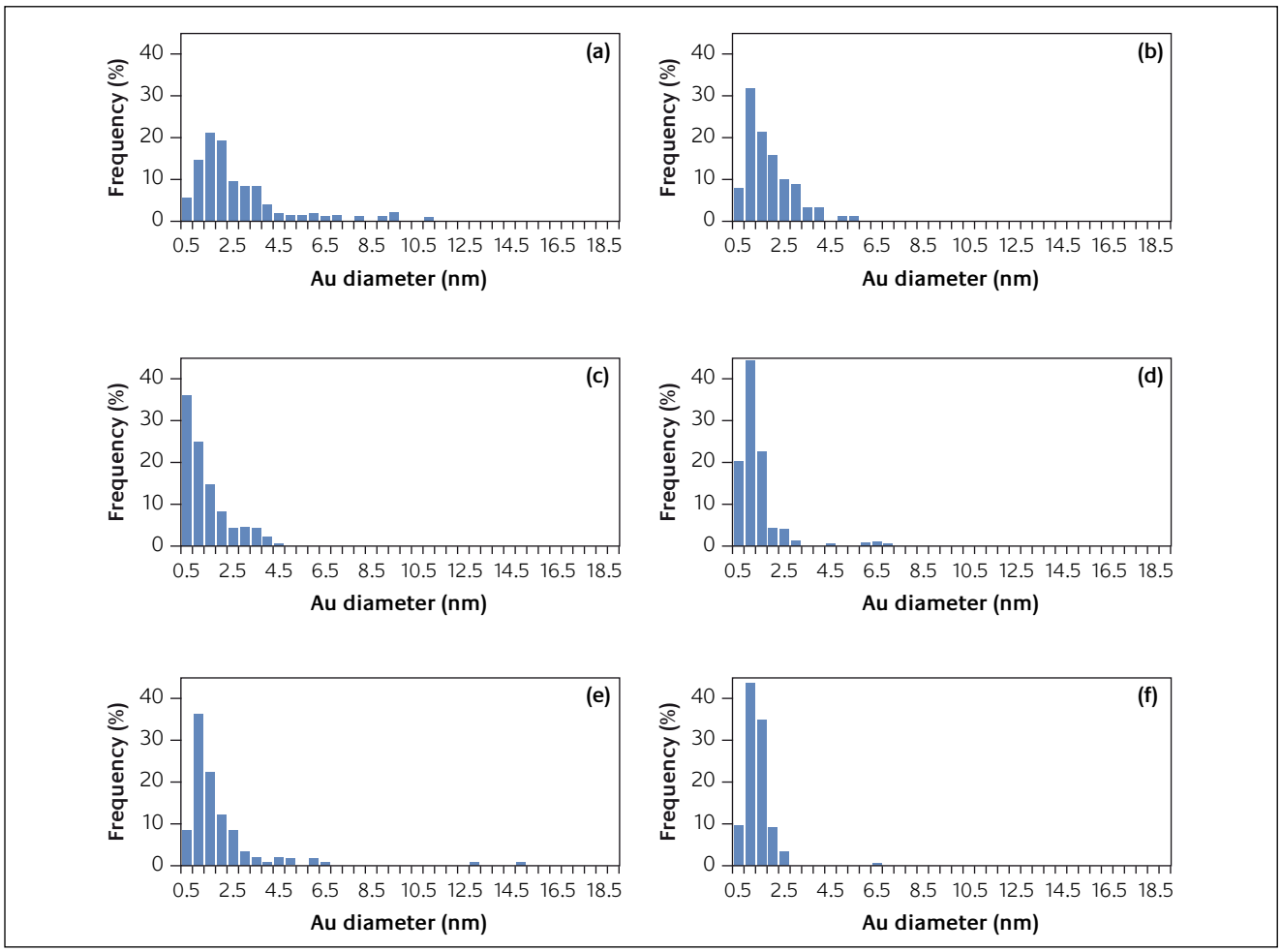

Figure 12

Gold particle size distributions of fresh and spent gold catalysts (a) & (b) Au9A, (c) & (d) Au9M and (e) & (f) AuUV100.

The AuUV100 catalyst displays the highest initial CO conversion rate compared to Au9A and Au9M catalysts. However, it lost half of its initial activity (i.e., from 0.15 to 0.07 mmol $s^{-1}g_{Au}^{-1}$) after 5 h of reaction (Figure 13a). It deactivated further with reaction as shown in the CO conversion plots in Figure 6c. The deactivation is most likely caused by the build-up of monodentate carbonate species on the catalyst surface as shown in Figure 13d. This result clearly shows that larger support area does not necessarily results in an improved catalyst.

4 Concluding remarks

This work clearly showed that the TiO_2 support characteristics and properties play an important role on the catalytic activity and stability of Au/TiO_2 catalyst for ambient temperature CO oxidation reaction. The CO oxidation on the gold catalysts was carried out in an operando-DRIFTS set-up equipped with DRIFTS reactor cell connected on-line to CO gas analyser and gas chromatograph enabling real time monitoring of surface reaction and simultaneous rate measurements. Gold supported on rutile TiO_2 rapidly sintered during the reaction resulting in irreversible catalyst deactivation. This was due to the poor metal-support interaction and greater mobility of gold on rutile. On the other hand, gold on anatase TiO_2 redispersed during the reaction resulting in finer gold particles. A milder deactivation was observed for these catalysts and was mainly caused by the deposition of surface carbonates on the TiO_2 support. A large support surface area is important for preparing highly dispersed gold catalysts. However it also promotes carbonate deposition resulting in rapid catalyst deactivation as shown by AuUV100. Also, it was observed that a sufficiently large pore is needed to achieve uniform catalyst dispersion. Unsupported gold were observed on TiO_2 with small pore sizes. The study showed that Au13A supported on the 13 nm anatase TiO_2 gave the best catalyst reactivity and displayed the highest resistance against deactivation. Further work is necessary to clarify the role of surface hydroxyls on catalyst preparation (i.e., catalyst loading) and stability (i.e., sintering and carbonate deposition).

Acknowledgements

The authors are grateful for the research funding from the Innovation and Technology Commission of the Hong Kong SAR Government (ITS/176/01C), Veolia Environment (Veolia

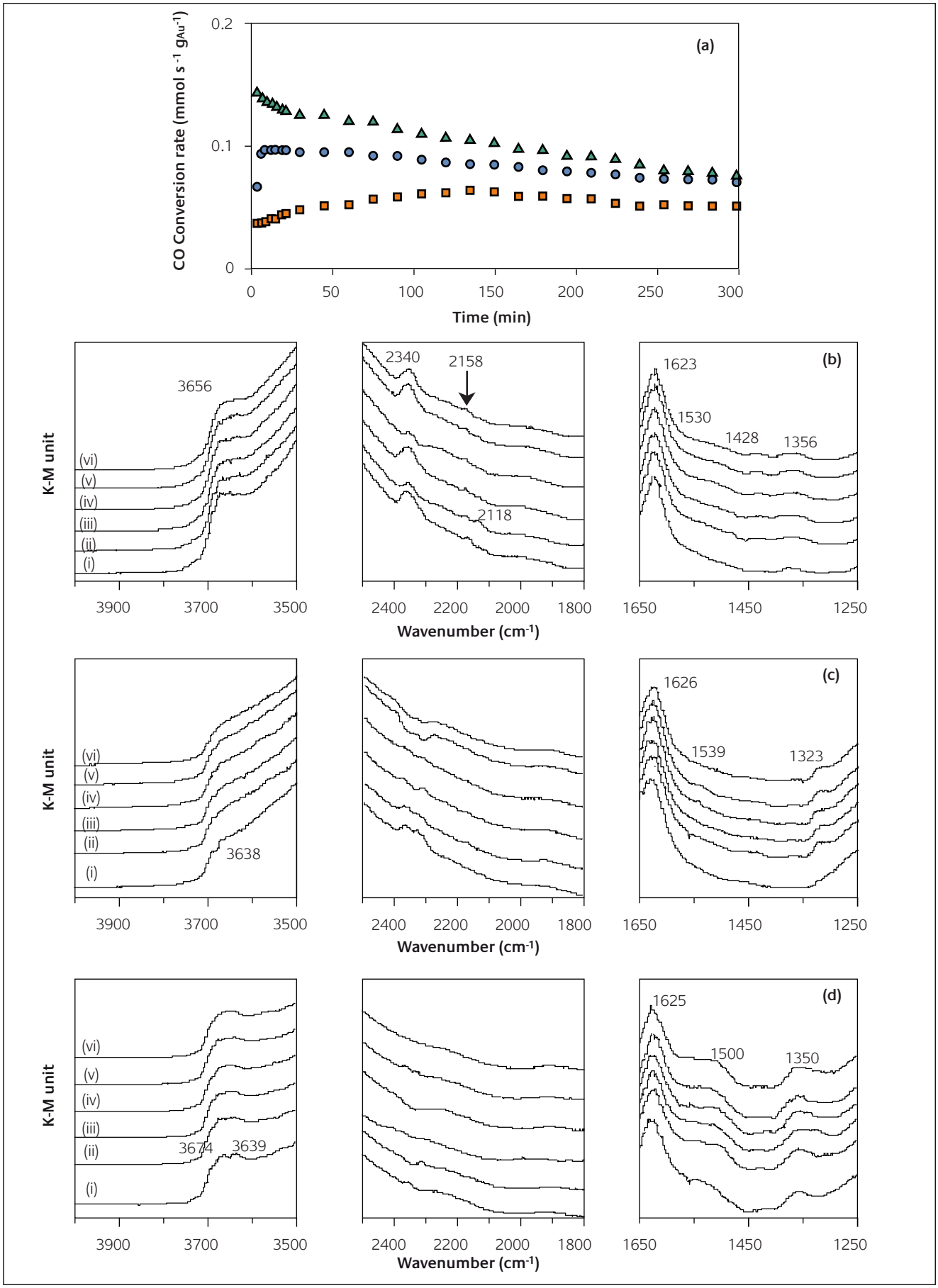

Figure 13

Operando-DRIFTS study of CO reaction on Au9A, Au9M and AuUV100 catalysts. (a) CO conversion rates versus time for Au9A (●), Au9M (■) and AuUV100 (▲) and DRIFTS spectra of CO reaction on (b) Au9A, (c) Au9M and (d) AuUV100 after reaction of 1 min (i), 60 min (ii), 120 min (iii), 180 min (iv), 240 min (v) and 300 min (vi).

Water Asia and Anjou Recherches), Honeywell HK, Chiaphua Industries Ltd. and Orkney Environmental Technology Ltd. Miss Alice Ho Ka Yee gratefully acknowledge the Postgraduate Scholarship from the Environmental Engineering Program. We also thank the Material Preparation and Characterization Facility (MCPF) of the Hong Kong University of Science and Technology for the use of the XRD and TEM for the catalyst characterization.

About the Authors

Dr. King Lun Yeung is an Associate Professor of Chemical Engineering at the Hong Kong University of Science and Technology. He obtained his Ph.D. in Chemical Engineering at the University of Notre Dame, U.S.A. in the area of surface science and catalysis. His current research focuses on the rational design and molecular-level engineering of functional nanoporous and nanostructured materials with chemical, environmental and bio-related applications.

Dr. Ka Yee HO is a PhD graduate from Prof. K L Yeung's research group. She is now working in the research and development of nanomaterials for Artenano Company Limited, Hong Kong.

References

1 M. Haruta, N. Yamada, T. Kobayashi, S. Iijima, J. Catal. 1989, **115**, 301
2 M. Haruta, S. Tsubota, T. Kobayashi, H. Kageyama, M.J. Genet, B. Delmon, J. Catal. 1993, **144**, 175
3 M. Valden, X. Lai, D.W. Goodman, Science 1998, **281**, 1647
4 G.C. Bond, D.T. Thompson, Cat. Rev. – Sci. Eng. 1999, **41**, 319
5 G.C. Bond, D.T. Thompson, Gold Bull. 2000, **33**, 41
6 M. Haruta, Chem. Rec. 2003, **3**, 75
7 M. Haruta, Gold Bull. 2004, **37**, 27
8 R. Zanella, S. Giorgio, C.R. Henry, C. Louis, J. Phys. Chem. B 2002, **106**, 7634
9 R. Zanella, S. Giorgio, C.H. Shin, C.R. Henry, C. Louis, J. Catal. 2004, **222**, 357
10 F. Moreau, G.C. Bond, A.O. Taylor, J. Catal. 2005, **231**, 105
11 F. Boccuzzi, A. Chiorino, M. Manzoli, P. Lu, T. Akita, S. Ichikawa, M. Haruta, J. Catal. 2001, **202**, 256
12 M. Maciejewski, P. Fabrizioli, J.D. Grunwaldt, O.S. Becker, A. Baiker, Phys. Chem. Chem. Phys. 2001, **3**, 3846
13 M. Daté, Y. Ichihashi, T. Yamashita, A. Chiorino, F. Boccuzzi, M. Haruta, Catal. Today 2002, **72**, 89
14 M. Haruta, M. Daté, Appl. Catal. A 2001, **222**, 427
15 L.M. Molina, B. Hammer, Appl. Catal. A 2005, **291**, 21
16 X. Zhang, H. Wang, B. Xu, J. Phys.Chem. B 2005, **109**, 9678
17 J.J. Pietron, R.M. Stroud, D.R. Rolison, Nano Lett. 2002, **2**, 545
18 D.R. Rolison, Science 2003, **299**, 1698
19 W. Yan, B. Chen, S.M. Mahurin, V. Schwartz, D.R. Mullins, A.R. Lupini, S.J. Pennycook, S. Dai, S.H. Overbury, J. Phys. Chem. B 2005, **109**, 10676
20 F. Moreau, G.C. Bond, Appl. Catal. A 2006, **302**, 110
21 A.J. Maira, K.L. Yeung, C.Y. Lee, P.L. Yue, C.K. Chan, J. Catal. 2000, **192**, 185
22 A.J. Maira, K.L. Yeung, J. Soria, J.M. Coronado, C. Belver, C.Y. Lee and V. Augugliaro, Appl. Catal. B 2001, **29**, 327
23 K.L. Yeung, A.J Maira, J. Stolz, E. Hung, N.K.C. Ho, A.C. Wei, J. Soria, K.J. Chao, P.L Yue, J. Phys. Chem. B 2002, **106**, 4608
24 A.J. Maira, J.M. Coronado, V. Augugliaro, K.L. Yeung, J.C. Conesa, J. Soria, J. Catal. 2001, **202**, 413w
25 K.L. Yeung, S.T. Yau, A.J. Maira, J.M. Coronado, J. Soria, P.L Yue, J. Catal. 2003, **219**, 107
26 S. Komarneni, R.K. Rajha, H. Katsuki, Mat.Chem. Phys. 1999, **61,** 50.
27 S. Karvinen, Solid State Sci. 2003, **5**, 811
28 W. Wang, B. Gu, L. Liang, W.A. Hamilton, D.J. Wesolowski, J. Phys. Chem. B 2004, **108**, 14789
29 R. Chu, J. Yan, S. Lian, Y. Wang, F. Yan, D. Chen, Solid State Commun. 2004, **130**, 789
30 J.N. Hart, R. Cervini, Y.B. Cheng, G.P. Simon, L. Spiccia, Sol. Energy Mater. Sol. Cells 2004, **84**, 135
31 H. Zhang, J.F. Banfield, J. Phys. Chem. B 2000, **104**, 3481
32 K.Y. Ho, K.L. Yeung, J. Catal. 2006, **242**, 131
33 J. Lynch, Physico-chemical analysis of industrial catalysts: A practical guide to characterization, Editions Technip, Paris, 2003, p. 8-9
34 J.M.C. Soares, P. Morrall, A. Crossley, P. Harris, M. Bowker, J. Catal. 2003, **219**, 17
35 M. Primet, P. Pichat, M. V. Mathieu, J. Phys Chem. 1971, **75**, 1216
36 K. Tanaka, J.M. White, J. Phy. Chem. 1982, **86**, 4708
37 P.P. Lottici, D. Bersani, M. Braghini, A. Montenero, J. Mater. Sci. 1993, **28**, 177
38 C. Morterra, J. Chem. Soc. Faraday Trans 1988, **84**, 1617
39 A.A. Davidov, Infrared Spectroscopy of Adsorbed Species on the Surface of Transition Metal Oxides, ed. C.H. Rochester, Wiley, Chichester, 1990, p. 39
40 M.A. Bollinger, M.A. Vannice, Appl. Catal. B 1996, **8**, 417
41 W.F. Zhang, Y.L. He, M.S. Zhang, Q. Chen, J. Phys. D 2000, **33**, 912
42 E. Barborini, I.N. Kholmanov, A.M. Conti, P. Piseri, S. Vinati, P. Malani, C. Ducati, Eur. Phys. J. 2003, **24**, 277
43 D. Bersani, P.P. Lottici, X.Z. Ding, Appl. Phys. Lett. 1998, **71**, 73
44 J.R. Anderson, M. Boudart, Catalysis: Science and Technology, Springer-Verlag, Berlin, 1984, p.247-248
45 G. Ertl, H. Knzinger, J. Weitkamp (Eds.), Preparation of Solid Catalysts, Wiley-VCH, Weinheim, 1999, p. 553
46 K.L. Yeung, E.E. Wolf, Catal. Lett. 1992, **12**, 213
47 K.L. Yeung, E.E. Wolf, J. Catal. 1992, **135**, 13
48 K.L. Yeung, E.E. Wolf, J. Vac. Sci. Technol. A 1992, **10**, 651
49 C.Y. Lee, A. Gavrildic, Q.A. Pankhurst, A. Kyek, F.E. Wagner, R.C.L. Wong, K.L. Yeung, J. Catal. 2001, **200**, 298